Optics Letters

Extended depth-of-field microscopy with a high-speed deformable mirror

William J. Shain,[1,2,*] Nicholas A. Vickers,[2,3] Bennett B. Goldberg,[1,4] Thomas Bifano,[2,3] and Jerome Mertz[2,5]

[1]Department of Physics, Boston University, 590 Commonwealth Avenue, Boston, Massachusetts 02215, USA
[2]Photonics Center, Boston University, 8 Saint Mary's St., Boston, Massachusetts 02215, USA
[3]Department of Mechanical Engineering, Boston University, 110 Cummington Mall, Boston, Massachusetts 02215, USA
[4]Searle Center for Advanced Learning and Teaching, Northwestern University, 627 Dartmouth Place, Evanston, Illinois 60208, USA
[5]Department of Biomedical Engineering, Boston University, 44 Cummington Mall, Boston, Massachusetts 02215, USA
*Corresponding author: shaine@bu.edu

Received 9 January 2017; revised 8 February 2017; accepted 9 February 2017; posted 9 February 2017 (Doc. ID 284343); published 28 February 2017

We present a wide-field fluorescence microscopy add-on that provides a fast, light-efficient extended depth-of-field (EDOF) using a deformable mirror with an update rate of 20 kHz. Out-of-focus contributions in the raw EDOF images are suppressed with a deconvolution algorithm derived directly from the microscope 3D optical transfer function. Demonstrations of the benefits of EDOF microscopy are shown with GCaMP-labeled mouse brain tissue.

OCIS codes: (180.2520) Fluorescence microscopy; (110.1080) Active or adaptive optics; (100.1830) Deconvolution.

https://doi.org/10.1364/OL.42.000995

In many fluorescence microscopy applications, it is important to image large volumes at high speed. In brain imaging, for example, neuronal signals can vary at millisecond timescales [1,2], with communicating neurons often separated by hundreds of microns. Imaging such fast dynamics over extended volumes presents a challenge for standard wide-field fluorescence microscopes [3]; while cameras with kilohertz frame rates are available, these provide only 2D snapshots. Fortunately, quasi 3D imaging can be obtained by extending the depth-of-field (DOF). For example, pupil engineering can achieve DOFs up to a few tens of microns without requiring any moving parts [4–12]. Extended depth-of-fields (EDOFs) can also be obtained by sweeping the sample [13] or by sweeping the focus using a remote mirror [14], an electrically tunable lens [15–18], or an acoustic gradient lens [19]. Another device attractive for this purpose is a MEMS deformable mirror (DM), which can offer kilohertz sweep rates [20] and the flexibility to be used for either focus control or an EDOF. We describe a simple, light-efficient technique for achieving fast, a single-shot EDOF with a DM configured as an add-on to a commercial microscope. The raw images produced by our device, while revealing all-in-focus information, also feature out-of-focus haze. This haze is removed by deconvolution using both an exact and approximated filter function derived directly from the microscope 3D optical transfer function (OTF).

Our setup is illustrated in Fig. 1. A conventional epifluorescence microscope projects a magnified image ($M = f_1/f_{\mathrm{obj}}$) of the sample onto an intermediate image plane, where a camera normally resides. In our case, the camera is set back, and the intermediate image plane is re-imaged onto the new camera plane using relay lenses f_2 and f_3, and a tilted DM is located in a plane conjugate to the microscope pupil plane. The purpose of tilting the DM (here ≈6°) is to avoid the use of a beam splitter and, thus, maximize light efficiency. This issue of light efficiency is often a major concern in fluorescence imaging and highlights a benefit of using a focal sweep rather than a low numerical aperture, for example, to obtain a large DOF.

Focus control is obtained by applying a parabolic shape to the DM, leading to an axial shift of the focal plane in the sample given by $Z = -nf_2^2/(M^2 f_{\mathrm{DM}})$, where f_{DM} is the focal length associated with the DM shape, and n is the index of the refraction in the sample [21]. The axial shift is thus related to the DM stroke S by

$$Z = \frac{4n^3}{\mathrm{NA}^2}\left(\frac{R_P}{R_{\mathrm{DM}}}\right)^2 S, \tag{1}$$

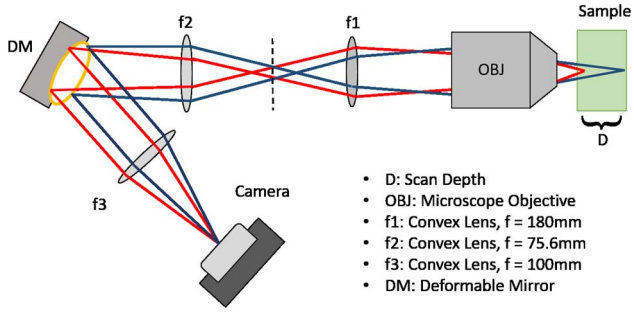

Fig. 1. Schematic of an EDOF microscope. The vertical dashed line indicates the location of the intermediate image plane.

where NA is the numerical aperture of the microscope objective, R_P is the radius of the objective pupil as imaged onto the DM plane, and R_{DM} is the radius of the active area on the DM. We note that R_P can be adjusted by changing f_2; this implies that, in principle, any DM diameter can be accommodated and, therefore, only the DM stroke affects the achievable DOF.

If f_2 is chosen such that $R_P = R_{\mathrm{DM}}$, applying a maximum stroke excursion of ΔS results in an EDOF given by $D = 4n^3\Delta S/\mathrm{NA}^2$. Since a standard wide-field microscope has a DOF approximately given by $D_0 = n\lambda/\mathrm{NA}^2$, the DM extends the DOF by a factor of $D/D_0 = 4n^2\Delta S/\lambda$. If f_2 is chosen differently, the objective pupil either underfills or overfills the active area of the DM. As observed from Eq. (1), underfilling reduces the DOF, but causes no significant change in image resolution; overfilling results in a larger DOF, but leads to the clipping of the higher spatial frequency components.

For our demonstrations, we used an Olympus BX51 microscope, adapted with a 140-actuator Multi-DM from Boston Micromachines Corporation (BMC). A BMC X-Driver with 20 kHz refresh rate was used to control the DM curvature, applying bi-directional strokes anywhere between fully convex and fully concave, with a maximum stroke excursion $\Delta S = 4.8$ μm, and over an active area ranging from 3 to 4 mm. Both an Olympus 20 × 0.5 NA air-immersion objective and an Olympus 40 × 0.8 NA water-immersion objective were used to image the samples, providing maximum expected DOF enhancements of about 40× and 70×, respectively. A Thorlabs M470 L3-C Blue LED was used for sample illumination, and a PCO Edge 4.2 LT camera for fluorescence image detection. To begin, we imaged 500 nm and 1 μm diameter fluorescent beads embedded in polydimethylsiloxane [PDMS (Fig. 2)], demonstrating the refocusing of out-of-plane beads consistent with the extension in the DOF. For high-speed imaging, we imaged 4 μm beads. Our maximum frame rate in this case was limited by our camera to 472 fps with a reduced field-of-view. We also restricted our camera to 1 ms exposure times (Fig. 3), thus confirming the potential of operating at a 1 kHz frame rate with a faster camera.

A difficulty with wide-field microscopy is that it does not provide optical sectioning. That is, in-focus images are generally contaminated with an out-of-focus background. The same is true when extending the DOF of a widefield microscope. All-in-focus images become contaminated with all-out-of-focus background, leading to a background haze that worsens as D increases. While the presence of this haze is not troublesome when the sample is sparse (see Fig. 3), it can become highly problematic when the sample is dense, causing sample features to become indistinguishable. A strategy to mitigate this problem of background haze is to use deconvolution. Specifically, the 3D PSF associated with an EDOF is largely independent of depth and, thus, to a good approximation, can be reduced to a representative extended 2D PSF [17]. The corresponding representative extended 2D OTF (or EOTF) required for deconvolution can then be obtained from this by Fourier transform. Alternatively, EOTF can be derived directly from the 3D OTF, taking advantage of the fact that the 3D OTF can be expressed analytically under the paraxial approximation for a circular unobstructed pupil. We adapt this expression from [22]

$$\mathrm{OTF}(\boldsymbol{\kappa}_\perp, \kappa_z) = \frac{4\kappa}{\pi\kappa_\perp\Delta\kappa_\perp}\sqrt{1-\left(\frac{2\kappa|\kappa_z|}{\kappa_\perp\Delta\kappa_\perp}+\frac{\kappa_\perp}{\Delta\kappa_\perp}\right)^2}, \quad \textbf{(2)}$$

where $\kappa = n/\lambda$ is the wavenumber, and $\Delta\kappa_\perp = 2\ \mathrm{NA}/\lambda$ is the pupil bandwidth. Equation (2) is valid for lateral spatial frequencies in the range $|\boldsymbol{\kappa}_\perp| = \kappa_\perp \le \Delta\kappa_\perp$ and axial spatial frequency in the range $|\kappa_z| \le \frac{\kappa_\perp}{2\kappa}(\Delta\kappa_\perp - \kappa_\perp)$; otherwise, it is zero.

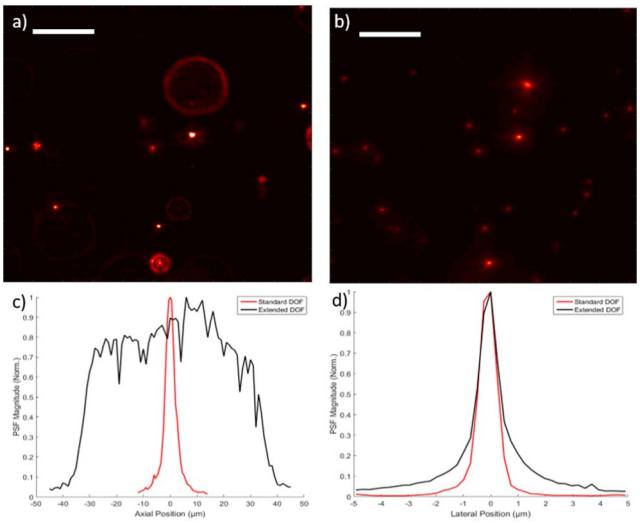

Fig. 2. Standard versus EDOF imaging of 1 μm diameter fluorescent beads embedded in PDMS. Images taken with a 20 × 0.5 NA objective; $R_P = 2.21$ mm, $R_{\mathrm{DM}} = 2$ mm, and the EDOF = 69 μm [Eq. (1)] with 26 DM frames. The beads that are out of focus in (a) the standard image appear focused in (b) the EDOF image, as illustrated by (c) the normalized axial PSFs. The measured EDOF obtained with beads on a slide is about 64 μm, roughly consistent with Eq. (1). A comparison of the lateral PSFs is shown in (d), illustrating that, while the EDOF does not significantly worsen lateral resolution, it causes an increase in the surrounding haze. The scale bar is 25 μm.

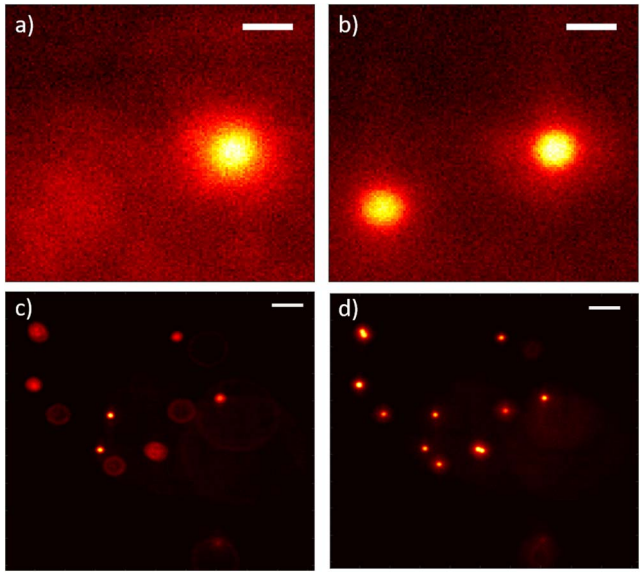

Fig. 3. High-speed images of 4 μm diameter beads. (a) Standard and (b) extended DOFs taken at 472 fps in a reduced field-of-view with a 40 × 0.8 NA objective; $R_P = 1.44$ mm, $R_{\mathrm{DM}} = 1.5$ mm, and the EDOF = 41 μm Eq. (1) with 26 DM frames. (Note that both beads in panel (a) are out of focus.) The scale bar is 5 μm. (c) Standard and (d) extended DOFs at 1 ms exposure with 20 × 0.5 NA objective; the EDOF = 69 μm with 20 DM frames. The scale bar is 25 μm.

Furthermore, it is normalized so that $\int \mathrm{OTF}(\boldsymbol{\kappa}_\perp, \kappa_z)\mathrm{d}\kappa_z$, which corresponds to the in-focus 2D OTF, is equal to unity when $\kappa_\perp \to 0$.

To derive a representative EDOF associated with an axial scan range D, we first take an inverse Fourier transform of the 3D OTF with respect to κ_z, as described in [23], and then average this over the scan range, obtaining

$$\begin{aligned}\mathrm{EOTF}(\boldsymbol{\kappa}_\perp; D) &= \int_{-\frac{D}{2}}^{\frac{D}{2}} \frac{\mathrm{d}z}{D} \int \mathrm{d}\kappa_z e^{i2\pi\kappa_z z}\mathrm{OTF}(\boldsymbol{\kappa}_\perp, \kappa_z) \\ &= \int \mathrm{d}\kappa_z \mathrm{sinc}(\kappa_z D)\mathrm{OTF}(\boldsymbol{\kappa}_\perp, \kappa_z). \end{aligned} \tag{3}$$

This expression is exact; however, its numerical integration is not always straightforward. We thus adopt a few approximations.

To begin, we consider the limit of $D \to 0$. In this case, we have

$$\mathrm{EOTF}(\boldsymbol{\kappa}_\perp; D) \to \int_{-\frac{\kappa_\perp}{2k}(\Delta\kappa_\perp - \kappa_\perp)}^{\frac{\kappa_\perp}{2k}(\Delta\kappa_\perp - \kappa_\perp)} \mathrm{d}\kappa_z \mathrm{OTF}(\boldsymbol{\kappa}_\perp, \kappa_z). \tag{4}$$

This can be verified to be equal to the in-focus 2D OTF, as expected. In particular, we have chosen to normalize our 3D OTF so that $\mathrm{EOTF}(\boldsymbol{\kappa}_\perp; D) \to 1$ as $\kappa_\perp \to 0$.

We now consider the limit $D \to \infty$. For this, we write $\mathrm{sinc}(\kappa_z D) \to \frac{1}{D}\delta(\kappa_z)$. The integration of Eq. (3) now becomes trivial; however, the result remains ill-defined in the low frequency limit $\kappa_\perp \to 0$. Following a similar procedure described in [21], we can simply replace this low frequency limit with its known value of unity at $\kappa_\perp = 0$, based on the normalization of our 3D OTF. Alternatively, we can do better by noting that the frequency support of $\mathrm{EOTF}(\boldsymbol{\kappa}_\perp; D)$ is expected to be no greater than that of the in-focus 2D OTF. In other words, we can write

$$\mathrm{EOTF}(\boldsymbol{\kappa}_\perp; D) \approx \min\left\{ \begin{array}{l} \int \mathrm{d}\kappa_z \mathrm{OTF}(\boldsymbol{\kappa}_\perp, \kappa_z) \\ \frac{1}{D}\mathrm{OTF}(\boldsymbol{\kappa}_\perp, 0), \end{array} \right. \tag{5}$$

or, written out explicitly,

$$\mathrm{EOTF}(\boldsymbol{\kappa}_\perp; D) \approx \min\left\{ \begin{array}{l} \frac{2}{\pi}\left(\cos^{-1}\eta - \eta\sqrt{1-\eta^2}\right) \\ \frac{4\kappa}{\pi D\Delta\kappa_\perp^2\eta}\sqrt{1-\eta^2}, \end{array} \right. \tag{6}$$

where $\eta = \kappa_\perp/\Delta\kappa_\perp$. This provides a good approximation to the exact integration of Eq. (3) for both large and small values of D (see Fig. 4).

In principle, a raw EDOF image $I(\boldsymbol{\rho})$ can be deconvolved to recover a corrected EDOF object $O(\boldsymbol{\rho})$ by simple Fourier transformation and division by $\mathrm{EOTF}(\boldsymbol{\kappa}_\perp; D)$ (where $\boldsymbol{\rho}$ are lateral spatial coordinates). A key advantage of $\mathrm{EOTF}(\boldsymbol{\kappa}_\perp; D)$ is that it contains no zeros within its bandwidth $\Delta\kappa_\perp$, rendering the deconvolution more stable. Nevertheless, unacceptable divergences can occur in the presence of image noise close to or beyond the bandwidth limit. To correct for this, we adopt the standard approach of regularization [17,24]. That is, we write

$$O(\boldsymbol{\rho}) = \mathcal{F}^{-1}\left[\frac{\mathrm{EOTF}(\boldsymbol{\kappa}_\perp; D)^*}{|\mathrm{EOTF}(\boldsymbol{\kappa}_\perp; D)|^2 + \varepsilon}\mathcal{F}[I(\boldsymbol{\rho})]\right], \tag{7}$$

where $\mathcal{F}$ corresponds to a Fourier transform, and $0 < \varepsilon \ll 1$ is a regularization parameter. The optimal value of ε can be rigorously determined based on the level of noise in $I(\boldsymbol{\rho})$. Here, we simply select it by eye.

The deconvolution in Eq. (7) was implemented in MATLAB by directly calculating the approximation of Eq. (6). For comparison, Mathematica was used to numerically integrate Eq. (3) to represent the exact EOTF. The two forms of the EOTF obtain virtually identical results, significantly improving the image quality and contrast compared to the pre-deconvolved EDOF image (Fig. 5).

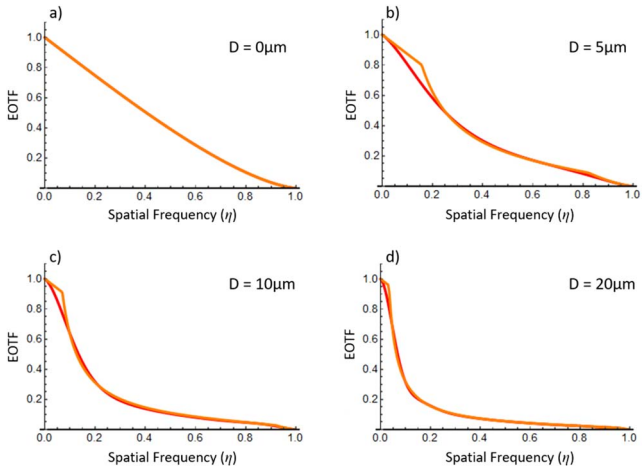

Fig. 4. $\mathrm{EOTF}(\boldsymbol{\kappa}_\perp; D)$ for a 20 × 0.5 NA objective for focal sweep ranges D of (a) 0, (b) 5, (c) 10, and (d) 20 μm. The EOTF calculated using Eq. (6) (orange) is a good approximation to the exact EOTF obtained by the numerical integration of Eq. (3) (red) for all values of D.

Finally, we demonstrate the benefits of an EDOF by imaging GCaMP-labeled neurons in a fixed mouse brain slice. Our frame rate, in this case, was limited by the signal intensity, as well as by the camera speed, since the fluorescence from the brain tissue was weaker than that of the 4 μm beads. This limitation could be alleviated somewhat by de-magnifying the image such that each neuron occupies only one or two

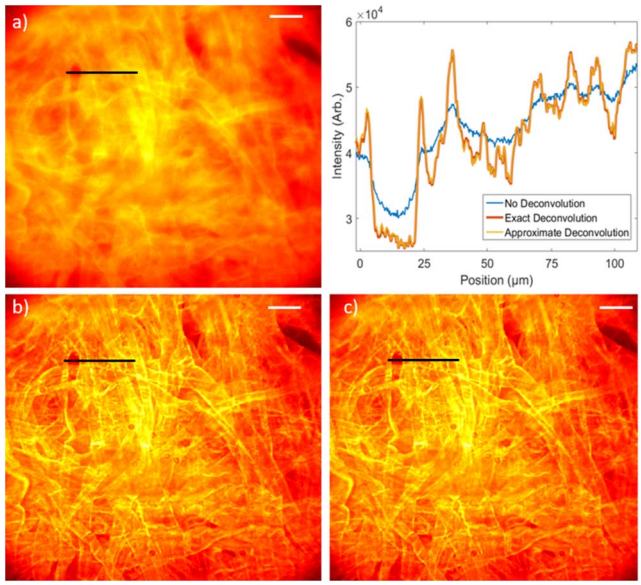

Fig. 5. Images of tissue paper labeled with a highlighter marker, taken with a 20 × 0.5 NA objective; the EDOF = 69 μm with 26 DM frames. (a) Raw EDOF image has poor contrast and few distinguishable features. Deconvolution using (b) exact EOTF numerically integrated from Eq. (3) and (c) approximate EOTF given by Eq. (6) results in similar images with a higher contrast, as seen in the line scan. Regularization parameter: $\varepsilon = 0.0056$. The scale bar is 50 μm.

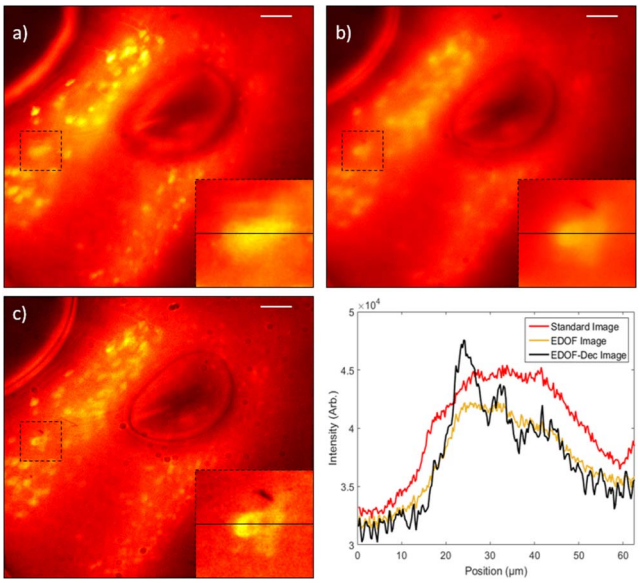

Fig. 6. Images of GCaMP-labeled mouse brain neurons taken with a 20 × 0.5 NA objective; the EDOF = 69 μm with 26 DM frames. (a) Standard image shows an out-of-focus neuron in the marked area. (b) With the EDOF, the neuron image becomes depth invariant but blurred. (c) After applying deconvolution based on Eq. (6), the neuron is in focus and the neuron body, including its nucleus, becomes clearly resolved. The line scans of the marked area illustrate improved contrast. Deconvolution parameter: $\varepsilon = 0.0056$. The scale bar is 50 μm.

camera pixels, thus mitigating the problem of readout noise. Nevertheless, even without this, we show much-improved imaging of out-of-focus neurons at high resolution (Fig. 6).

A unique feature of this approach for an EDOF is that the DM can, in principle, provide aberration corrections on the fly [20]. Such aberrations can occur when imaging through a strong index of refraction mismatch; for example, spherical aberration can occur when imaging mouse tissue using a high-NA microscope. Aberrations can also occur due to physical variations in the sample the tilt of the DM itself though, for small tilt angles, these are small (here $\lesssim \lambda/14$) and essentially negligible [25]. In our demonstrations, we do not exploit this potential advantage. Instead, we concentrate on the advantages of speed and versatility provided by a DM that can supply a user-defined number and range of curvatures at 20 kHz refresh rates with different objectives, and a high light efficiency that avoids diffraction or beam splitter losses.

Funding. National Science Foundation (NSF) (IIP-1068070); National Institutes of Health (NIH) (R01CA182939).

Acknowledgment. The authors thank Lei Tian and Anne Sentenac for helpful discussions. They are also grateful to the Jason Ritt laboratory for supplying brain tissue samples. Professor Bifano acknowledges a financial interest in Boston Micromachines Corporation.

REFERENCES

1. Y. Gong, C. Huang, J. Z. Z. Li, B. F. Grewe, Y. Zhang, S. Eismann, and M. J. Schnitzer, Science **350**, 1361 (2015).
2. A. S. Abdelfattah, S. L. Farhi, Y. Zhao, D. Brinks, P. Zou, A. Ruangkittisakul, J. Platisa, V. A. Pieribone, K. Ballanyi, A. E. Cohen, and R. E. Campbell, J. Neurosci. **36**, 2458 (2016).
3. N. Ji, J. Freeman, and S. L. Smith, Nat. Neurosci. **19**, 1154 (2016).
4. W. T. Welford, J. Opt. Soc. Am. **50**, 749 (1960).
5. G. Indebetouw and H. Bai, Appl. Opt. **23**, 4299 (1984).
6. E. R. Dowski and W. T. Cathey, Appl. Opt. **34**, 1859 (1995).
7. A. Castro and J. Ojeda-Castaneda, Appl. Opt. **43**, 3474 (2004).
8. A. Greengard, Y. Y. Schechner, and R. Piestun, Opt. Lett. **31**, 181 (2006).
9. S. Abrahamsson, S. Usawa, and M. Gustafsson, Proc. SPIE **6090**, 60900N (2006).
10. E. E. García-Guerrero, E. R. Méndez, and H. M. Escamilla, Opt. Express **15**, 910 (2007).
11. K. Chu, N. George, and W. Chi, Appl. Opt. **47**, 6895 (2008).
12. S. Quirin, D. S. Peterka, and R. Yuste, Opt. Express **21**, 16007 (2013).
13. G. Hausler, Opt. Commun. **6**, 38 (1972).
14. E. Botcherby, R. Juskaitis, M. Booth, and T. Wilson, Opt. Lett. **32**, 2007 (2007).
15. H. Oku, K. Hashimoto, and M. Ishikawa, Opt. Express **12**, 2138 (2004).
16. B. F. Grewe, F. F. Voigt, M. van't Hoff, and F. Helmchen, Biomed. Opt. Express **2**, 2035 (2011).
17. S.-H. Lu and H. Hua, Opt. Express **23**, 10714 (2015).
18. M. Martínez-Corral, P.-Y. Hsieh, A. Doblas, E. Sánchez-Ortiga, G. Saavedra, and Y.-P. Huang, J. Display Technol. **11**, 913 (2015).
19. A. Mermillod-Blondin, E. McLeod, and C. B. Arnold, Opt. Lett. **33**, 2146 (2008).
20. C. C. Archer-Zhang, W. B. Foster, R. D. Downey, C. L. Arrasmith, and D. L. Dickensheets, J. Biomed. Opt. **21**, 121507 (2016).
21. J. D. Giese, T. Ford, and J. Mertz, Opt. Express **22**, 1152 (2014).
22. B. Frieden, J. Opt. Soc. Am. **57**, 56 (1967).
23. C. Sheppard and M. Gu, J. Opt. Soc. Am. A **8**, 692 (1991).
24. J.-A. Conchello and M. E. Dresser, J. Biomed. Opt. **12**, 064026 (2007).
25. A. R. Bayanna, R. Louis, S. Chatterjee, S. Mathew, and P. Venkatakrishnan, Appl. Opt. **54**, 1727 (2015).